



# Facile synthesis and an effective doping method for ZnO:In<sup>3+</sup> nanorods with improved optical properties



Giwoong Nam, Byunggu Kim, Jae-Young Leem\*

Department of Nanoscience & Engineering, Inje University, 197, Inje-ro, Gimhae-si, Gyeongsangnam-do 621-749, Republic of Korea

## ARTICLE INFO

### Article history:

Received 10 March 2015

Received in revised form

11 August 2015

Accepted 13 August 2015

Available online 15 August 2015

### Keywords:

Oxide materials

Nanostructured materials

Sol-gel process

Optical properties

## ABSTRACT

The sol-gel spin-coating method is usually used for thin-film deposition rather than to grow one-dimensional nanostructures. In this study, a novel regrowth method for spin-coated ZnO:In<sup>3+</sup> films is demonstrated, using vapor-confined face-to-face annealing (VC-FTFA) in which a mica sheet is inserted between the two films prior to FTFA. ZnO:In<sup>3+</sup> nanorods are regrown when indium chloride is used as the solvent because ZnCl<sub>2</sub> and InCl<sub>3</sub> vapors are generated and confined between the films. The near-band-edge emission intensity of the ZnO:In<sup>3+</sup> nanorods resulting from VC-FTFA at 700 °C is enhanced by a factor of 17 compared with that of ZnO:In<sup>3+</sup> films annealed in open air at the same temperature. Our method offers a simple and low-cost route for the fabrication of ZnO nanorods.

© 2015 Elsevier B.V. All rights reserved.

## 1. Introduction

ZnO is one of the most promising materials for the fabrication of optoelectronic devices operating in the blue and ultraviolet (UV) regions [1–4], because of a wide direct band gap ( $E_g = 3.37$  eV at room temperature) and a large exciton binding energy (60 meV), much larger than that of GaN (25 meV), as well as a thermal energy at room temperature (26 meV) that ensures efficient exciton emission under ambient conditions. Moreover, one-dimensional (1D) ZnO nanostructures, including nanorods, nanowires, and nanotubes, have aroused considerable research interest in many areas of nanoscience and nanotechnology. 1D nanostructures have unusual and unique physical properties with quantum-mechanical confinement effects (QCE) [5–7] and a high surface-to-volume ratio making them relevant for the development of new devices and sensors [8–10]. In particular, it is believed that QCE plays a crucial role in improving the optical properties of materials [11,12].

Intrinsic ZnO films are usually n-type semiconductors because of their native point defects, namely oxygen vacancies and Zn interstitials [13]. Their number can be reduced either by annealing the ZnO films in an oxygen atmosphere or by appropriate doping. Group III elements, such as Al, Ga, and In can be used as donor dopants for ZnO. Indium is an important dopant in ZnO whose

presence changes the conductivity of the n-type material; therefore, ZnO is doped with In to control resistivity for electrical applications, notably in UV photodetectors, field-effect transistors, solar cells, and gas sensors [14–17]. To date however, the ZnO:In<sup>3+</sup> films or nanostructures prepared in most studies exhibit poor photoluminescence (PL) properties [14,18–21]. Considerable efforts have been devoted to the synthesis of 1D ZnO nanostructures, and various approaches have been demonstrated for the fabrication of semiconducting ZnO nanowires or nanorods.

Metal-organic chemical vapor deposition, chemical vapor deposition, the hydrothermal method, electrochemical deposition, and chemical bath deposition have all been used to prepare ZnO nanorods [22–26]. Another option is the sol-gel spin-coating method, which is conventionally used to deposit thin film rather than to grow 1D nanostructures. Should it be adapted for the growth of nanorods however, this method offers better reproducibility, lower costs, and mass production capability.

A face-to-face annealing (FTFA) approach is commonly employed for GaAs semiconductors to prevent the out-diffusion of arsenic [27]. The GaAs wafer to be annealed is placed between a bottom Si wafer and a top GaAs wafer with the polished surfaces facing each other (hence the name of the method). In previous study, we grew the ZnO nanorods by vapor-confined FTFA (VC-FTFA) using magnesium chloride hexahydrate or zinc chloride [28,29]. In this study, we fabricate ZnO:In<sup>3+</sup> nanorods, using indium chloride to regrow the nanorods. The VC-FTFA method has several advantages over conventional FTFA methods; in particular, samples

\* Corresponding author.

E-mail address: [jyleem@inje.ac.kr](mailto:jyleem@inje.ac.kr) (J.-Y. Leem).

prepared by VC-FTFA show more intense the near-band-edge (NBE) emission in PL spectra. In this study, we describe the mechanism for the generation of vapor during annealing and the influence of the confined vapor during VC-FTFA on the optical properties of the ZnO:In<sup>3+</sup> nanorods.

## 2. Experimental procedures

### 2.1. Preparation of ZnO:In<sup>3+</sup> film

The precursor solutions for the ZnO:In<sup>3+</sup> films were prepared by dissolving zinc acetate dihydrate (4.302 g, Zn(CH<sub>3</sub>COO)<sub>2</sub>·2H<sub>2</sub>O, ACS Reagent, >98%, Sigma–Aldrich) and indium chloride (0.088 g, InCl<sub>3</sub>, 98%, Sigma–Aldrich) in 2-methoxyethanol (99.8%, Sigma–Aldrich) up to a total volume of 40 mL. The concentration of the metal precursors was 0.5 M. Monoethanolamine (C<sub>2</sub>H<sub>7</sub>NO, MEA, ACS Reagent, >99.0%, Sigma–Aldrich) was used as a stabilizing agent to improve the solubility of the precursor salt. The molar ratio of MEA to metal salts was 1.0 (1.204 mL), and the ratio of In to Zn was fixed to 2 at.%. The stabilized sol solution was stirred at 60 °C for 2 h until it became clear and homogeneous. It was subsequently cooled to room temperature and aged for 24 h before it was used as the coating solution to deposit the films. The p-Si substrates were ultrasonically cleaned in acetone and ethanol for 10 min, rinsed with deionized water, and blow-dried with nitrogen. The precursor solution was spin-coated onto a p-Si substrate at 2000 rpm for 20 s, and the films were then dried at 200 °C for 10 min in an oven. These spin-coating and drying procedures were repeated five times.

### 2.2. Fabrication of ZnO:In<sup>3+</sup> nanorods through regrowth

The basic strategy for annealing spin-coated ZnO films is illustrated in Fig. 1. Three samples were prepared at 700 °C for 1 h for a comparative study. Sample 1 was annealed in open air. Sample 2 was annealed using the conventional FTFA method, whereby two films are placed together in an FTF arrangement during annealing. For sample 3, a mica sheet was inserted between the two films, which were then annealed using the FTF method.

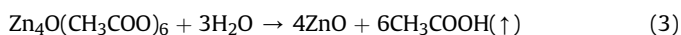
### 2.3. Characterization

PL spectra were measured at various temperatures in a He gas cryostat. The samples were excited using an unfocused 325 nm 20 mW He–Cd laser and the emitted photons were dispersed using a single monochromator with a 0.75-m focal length, and counted in a Hamamatsu R928 photomultiplier tube. The wavelength resolution of the PL system was 0.1 nm. The surface morphology of the samples was analyzed using field-emission scanning electron microscope (FE-SEM, HITACHI, S-4800). The thermal analysis of the zinc acetate dihydrate and zinc chloride/zinc acetate dihydrate precursors was performed by thermogravimetric-differential thermal analysis (TG-DTA, TA Instruments, SDT Q600) at a heating rate of 10 °C·min<sup>-1</sup> in air.

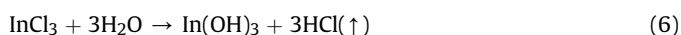
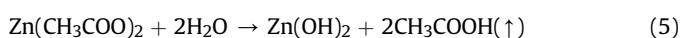
## 3. Results and discussion

The thermal-decomposition of the ZnO (zinc acetate dihydrate) and ZnO:In<sup>3+</sup> (indium chloride + zinc acetate dihydrate, In/Zn = 2 at.%) precursors was analyzed using TG-DTA to quantify their thermal stability and decomposition temperature; the materials were heated in air from room temperature up to 800 °C at 10 °C·min<sup>-1</sup>, as shown in Fig. 2. An initial endothermic reaction is observed for both precursors between 27 and 150 °C, amounting to 6.9% and 8.5% weight loss for ZnO and ZnO:In<sup>3+</sup> precursors, respectively, that arises from the thermal dehydration of zinc

acetate dihydrate, which becomes anhydrous. Further decomposition of the anhydrous zinc acetate causes weight loss near 150 °C and the decomposition process is completed by an exothermic reaction before 300 °C. The 61.5% weight loss measured here is greater than the 46.5% predicted theoretically. The extra 15.0% weight loss can be attributed to sublimation of zinc acetate species or to the formation of other volatile zinc organic compounds such as Zn<sub>4</sub>O(CH<sub>3</sub>COO)<sub>6</sub> [30,31]. As the temperature increases therefore, the ZnO precursor gradually decomposes to form ZnO through the following chemical reactions [31]:



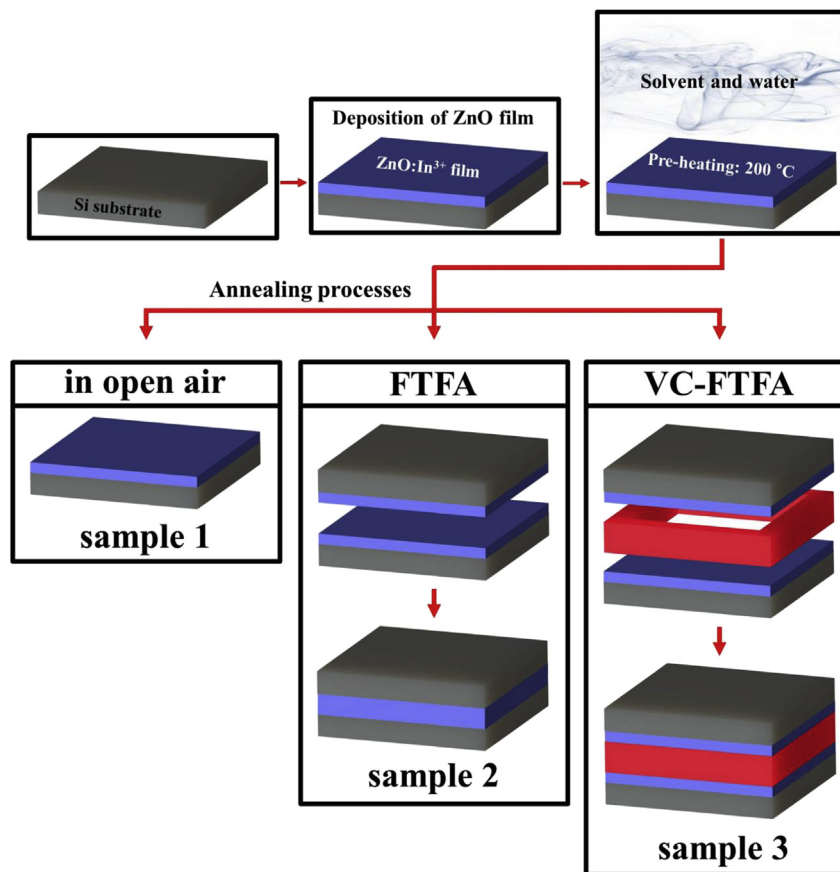
On the other hand, the ZnO:In<sup>3+</sup> precursor exhibits further weight loss in the 150–260 °C and 260–390 °C regions, due to the decomposition of organic compounds. Specifically, between 390 and 640 °C, the ZnO:In<sup>3+</sup> precursor slowly evaporates, generating ZnCl<sub>2</sub> and InCl<sub>3</sub> vapors, as described by the following reactions:



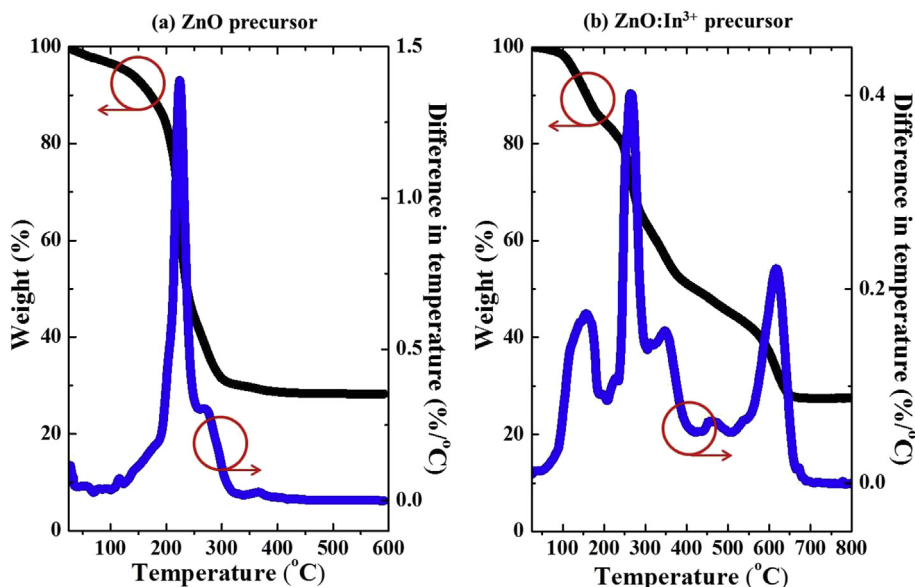
For the ZnO and ZnO:In<sup>3+</sup> precursors, endothermic and exothermic peaks are observed in the heat flow analysis of Fig. 2 between 25 and 330 °C and between 25 and 550 °C, respectively. These peaks are attributed to the evaporation of water and organics from these precursors. The last exothermic peaks in the TG-DTA curves of the zinc acetate dihydrate and zinc chloride/zinc acetate dihydrate precursors, respectively at 370 and 580 °C, result from the crystallization of ZnO.

The SEM image in Fig. 3(a) shows that the surface of sample 1 consists of numerous spherical ZnO:In<sup>3+</sup> particles approximately 100 nm in diameter. There are many dangling bonds on the surface of these samples before annealing, related to the oxygen vacancies of the grain boundaries. When annealed in open air, adjacent grains merge into larger particles approximately 100 nm in diameter. For samples 2 and 3, during FTFA and VC-FTFA respectively, ZnO:In<sup>3+</sup> nanorods grow from spherical ZnO:In<sup>3+</sup> seeds. ZnCl<sub>2</sub> and InCl<sub>3</sub> vapors are generated between 260 and 640 °C, leading to the regrowth of spherical nanoparticles. The nanorods in sample 3 are longer than those in sample 2. As shown in Fig. 3(b), the regrowth of the ZnO:In<sup>3+</sup> nanorods occurs through a vapor-solid mechanism, whereby nanorods grow via oxidation of the produced Zn vapor, which then condenses. ZnCl<sub>2</sub> and InCl<sub>3</sub> vapors decompose at 390–640 °C, and the Zn and In vapor adsorbed on the spherical nanoparticles with oxygen-containing organic compounds or with oxygen present in the air. In contrast, Fig. 3(c) shows that the surface morphology does not change when the ZnO:In<sup>3+</sup> films were prepared using an indium acetate precursor as dopant. The chemical reactions of indium acetate are similar to those of zinc acetate dihydrate but according to Equations (1–4), an acetate-based solvent does not generate the vapors that facilitate regrowth. ZnO:In<sup>3+</sup> nanorods therefore only form by regrowth when a chloride-based solvent is used, through the ZnCl<sub>2</sub> and InCl<sub>3</sub> vapors produced.

Fig. 4 shows the X-ray diffraction patterns of the three samples. Three ZnO diffraction peaks were observed at 31.9°, 34.7°, and



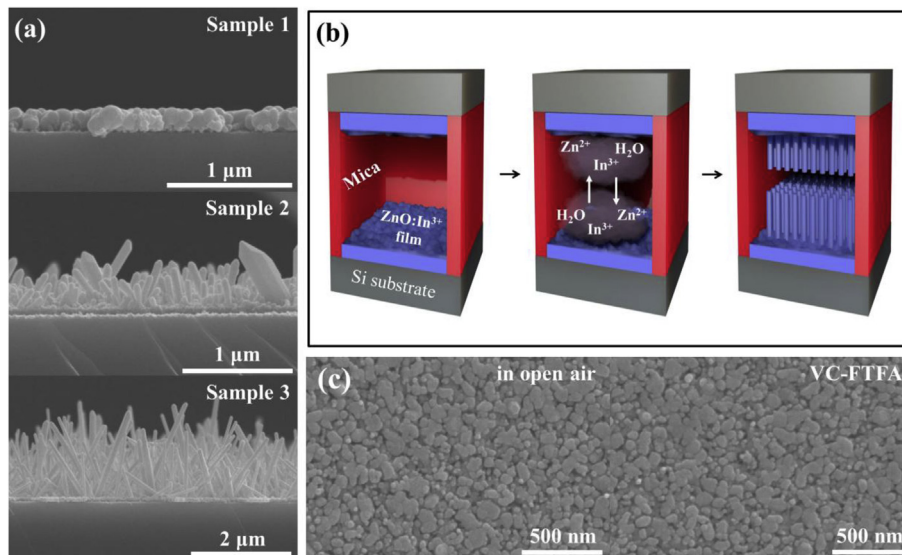
**Fig. 1.** Schematic diagram outlining the fabrication of the three samples investigated in this study. The effects of different annealing configurations were compared, viz. In open air (sample 1), FTFA (sample 2), and VC-FTFA for which an extra mica sheet is inserted between the two films (sample 3).



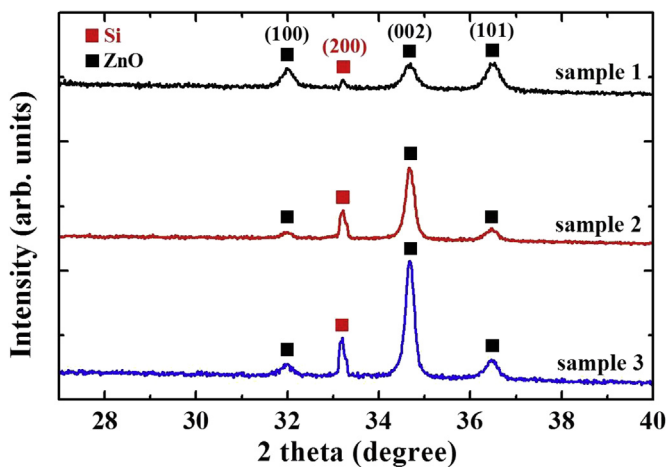
**Fig. 2.** TG-DTA curves obtained for the ZnO (left) and ZnO:In<sup>3+</sup> (right) precursors used in this study, respectively showing the weight loss percentage (in black) and the difference in temperature (in blue). (For interpretation of the references to colour in this figure legend, the reader is referred to the web version of this article.)

36.5°, which correspond to the (100), (002), and (101) planes, respectively. No traces of In metal or oxide were detected, indicating that the wurtzite structure was not modified by the incorporation of In into the ZnO matrix. Sample 2 and 3 exhibited a

strong (002) peak, indicating that the c-axis orientation of the ZnO grains was perpendicular to the substrate. It was also observed that the intensity of the (002) peak in sample 3 was larger than that in sample 2.



**Fig. 3.** (a) SEM images of ZnO:In<sup>3+</sup> films prepared by annealing in open air (sample 1), FTFA (sample 2), or VC-FTFA (sample 3). (b) Schematic illustration of the regrowth mechanism of ZnO nanorods by VC-FTFA. (c) SEM images of ZnO:In<sup>3+</sup> films prepared using indium acetate instead of indium chloride in the precursor and annealed at 700 °C in open air (left) or using VC-FTFA (right).



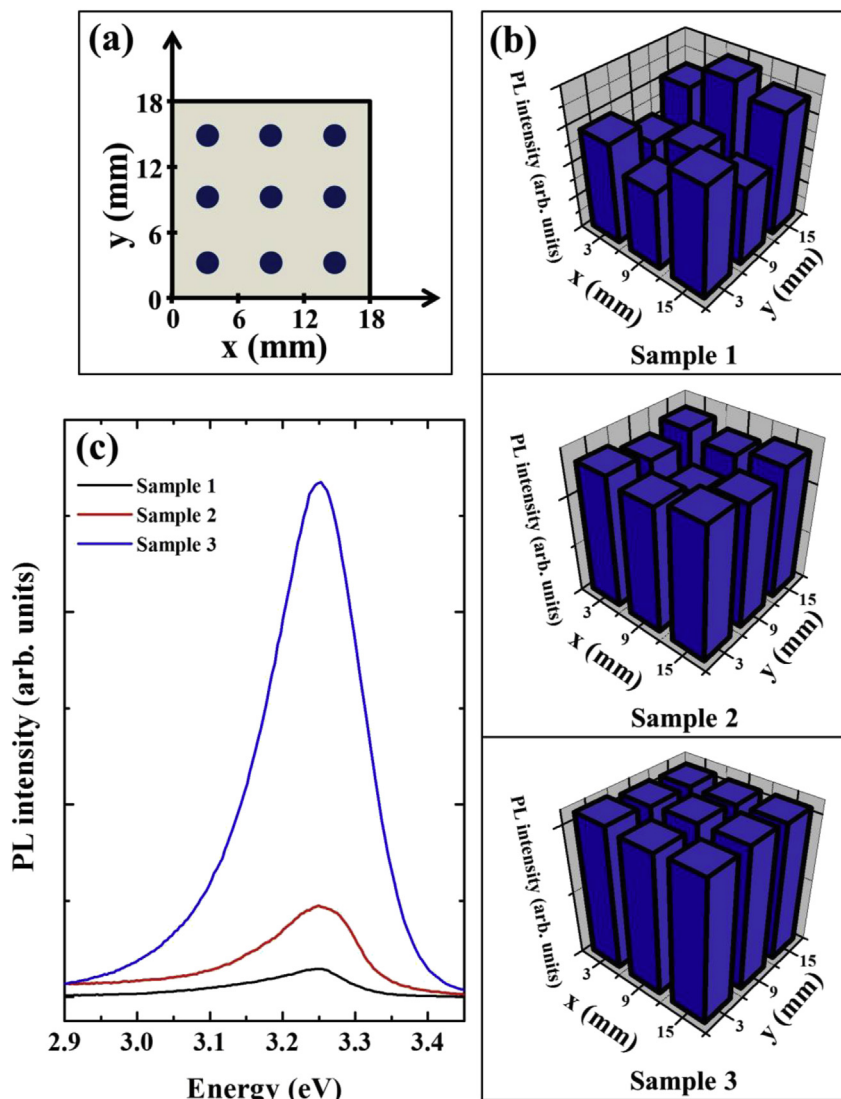
**Fig. 4.** XRD analysis of the three samples.

Fig. 5(b) shows the degree of uniformity of the NBE emission intensities in the PL spectra of the three samples using a continuous-wave He–Cd laser as the optical excitation source, as measured at the points marked in blue in Fig. 5(a). The NBE emission intensities vary randomly across the surface of sample 1, whereas for sample 2 the emission is stronger towards the edges of the sample due to insufficient confinement of the ZnCl<sub>2</sub> and InCl<sub>3</sub> vapors. Indeed, when these vapors remain too briefly at the center of the surface, only relatively small spherical nanoparticles are regrown. For sample 3 however, the NBE emission intensities are evenly distributed across the entire surface because in VC-FTFA, the vapors are confined by the mica sheet. We thereby attribute the active regrowth to the confinement of these vapors. Fig. 5(c) presents the PL spectra obtained for the three samples, with a NBE peak at 3.250 eV attributed to the ZnO:In<sup>3+</sup> phase. The NBE emission is clearly enhanced in sample 3, prepared by VC-FTFA, with a ZnO:In<sup>3+</sup> peak about 17 times more intense than sample 1, annealed in open air. These results show that VC-FTFA regrowth is effective in improving both the intensity and the uniformity of the

NBE emission. Fig. 6(a) shows that the NBE emission intensity from the ZnO:In<sup>3+</sup> films deposited using indium acetate precursor as a dopant and annealed in open air, is similar to that from films prepared by VC-FTFA method. However, the deep level (DL) emission from the latter is slightly lower than from the former. This result is similar to that reported by Wang et al. [32], and does not arise from regrowth. Chloride-containing metals, such as magnesium chloride (MgCl<sub>2</sub>), can generate ZnCl<sub>2</sub> and metal chloride vapors, and Fig. 6(b) shows that the resulting NBE emission is more intense and blue-shifted when annealing is performed in open air rather than by VC-FTFA.

Fig. 7 presents the PL spectra of ZnO:In<sup>3+</sup> films prepared by VC-FTFA at different temperatures from 400 to 800 °C. The NBE emission intensity increases for annealing temperatures up to 700 °C. The emission from the film annealed at 400 °C is the weakest, because the generation and decomposition of ZnCl<sub>2</sub> and InCl<sub>3</sub> is minimal at this temperature. At 700 °C on the contrary, ZnCl<sub>2</sub> and InCl<sub>3</sub> vapors are optimally generated and decomposed, resulting in active regrowth on the ZnO:In<sup>3+</sup> films through the confined vapors. Confinement fails however at 800 °C and the vapors escape, leading to weaker NBE emission from the films prepared at this temperature.

Fig. 8 shows the PL spectra recorded at 12 K for sample 3 and for an undoped ZnO film annealed in open air at 700 °C. Five distinct PL peaks appear in the spectra of the ZnO film, at 3.376, 3.361, 3.323, 3.251, and 3.036 eV. The first three of these are attributed to the emission of free excitons (FXs), neutral-donor-bound excitons (D<sup>0</sup>Xs), and two-electron satellites (TESs), respectively [33]. The peak at 3.251 eV is attributed to first-order longitudinal optical (LO) phonon replicas of TESs. In ZnO, the latter are generally identified based on the energy interval between the TES and the LO phonon energy ( $h\omega_{LO} = 72$  meV) [34]. The DL emission at 3.036 eV is attributed to a native zinc vacancy defect. In general, TESs are associated with D<sup>0</sup>X transitions occurring between 3.32 and 3.34 eV [33]. Bound excitons are extrinsic transitions related to dopants or defects, which usually create discrete electronic states in the bandgap. In theory, excitons could be bound to neutral or charged donors and acceptors. Shallow neutral donor-bound excitons often dominate because of the presence of donors from



**Fig. 5.** (a) Samples were measured at the points marked in blue to show NBE emission intensity uniformity. (b) The degree of NBE emission intensity uniformity in the PL spectra of the three samples. (c) PL spectra obtained from the three samples at 300 K. (For interpretation of the references to colour in this figure legend, the reader is referred to the web version of this article.)

unintentional impurities and/or shallow donor-like defects. During the recombination of the  $D^0X_s$ , the final state of the donor can either be  $1s$  (resulting in a normal  $D^0X$  line) or  $2s/2p$  (resulting in a  $TES_i$  line). The energy difference between the  $D^0X$  and its  $TES_i$  peaks therefore indicates the difference between the donor energies in the  $1s$  and  $2s/2p$  states. The donor excitation energy from the ground state to the first excited state is equal to  $3/4$  of the donor binding energy ( $E_D$ ) [33,35]. Here, the  $TES$  and  $D^0X$  peak positions indicate an  $E_D$  of 50.7 meV, the same value as estimated using Haynes' empirical rule [33]. Similarly, the binding energy of the neutral donor-bound excitons is estimated to be 15 meV from the energy difference between the FX and  $D^0X$  emissions, which is identical to the activation energy for thermal release of excitons from neutral donors. For sample 3, four distinct peaks are observed in the spectra, at 3.361, 3.356, 3.316, and 3.227 eV, which are attributed to FXs,  $D^0X_s$ , excitons bound to surface defects, and donor–acceptor pair transitions, respectively [36–39]. The  $D^0X$  peak is blue-shifted due to the incorporation of indium [39] and the emission at 3.316 eV is associated with the large surface-to-volume-ratio nanorods [40].

To identify the origin of these UV emissions, PL spectra were

recorded for sample 3 at temperatures from 12 to 300 K, as shown in Fig. 9(a). The  $D^0X$  peak is the most intense at 12 K but the FX emission becomes dominant above 75 K, indicating that the probability for the bound excitons to be ionized increases with the temperature. The UV emission of a ZnO crystal is usually attributed to the interband recombination of electrons and holes in form of excitons. Generally, due to the temperature-induced lattice dilatation and electron–lattice interaction, the interband emission peak energy follows the well-known Varshni formula [41]:

$$E_g(T) = E_g(0) - \alpha T^2 / (\beta + T), \quad (8)$$

where  $T$  is the absolute temperature,  $E_g(0)$  is the band-gap energy at  $T = 0$ ,  $\alpha$  and  $\beta$  are constants specific to ZnO, and  $\beta$  is proportional to the Debye temperature  $\theta_D$ . The  $\alpha$  and  $\beta$  values obtained from fitting the PL peaks of FX were  $\alpha = 1.1$  meV/K and  $\beta = 880$  K, as shown in Fig. 9(b). These values of  $\alpha$  and  $\beta$  well agree with those reported for the bulk ZnO semiconductor materials [42,43].

The intensities of all these PL peaks decrease with increasing temperature because of the thermally induced dissociation of

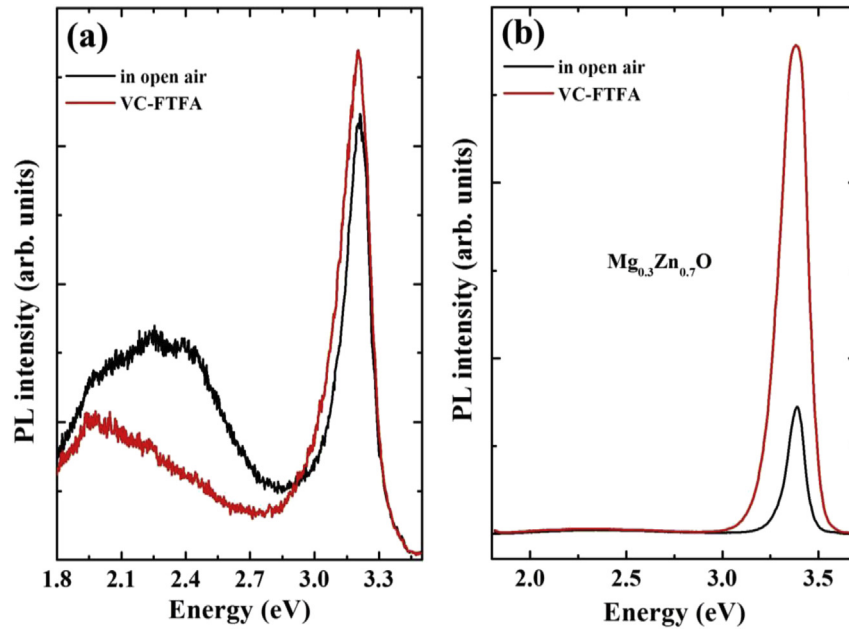


**Fig. 6.** PL spectra of ZnO:In<sup>3+</sup> films prepared using an indium acetate/zinc acetate dihydrate precursor and annealed at 700 °C in open air (black line) or by VC-FTFA (red line). (b) PL spectra of Mg<sub>0.3</sub>Zn<sub>0.7</sub>O annealed at 600 °C in open air (black line) or by VC-FTFA (red line). (For interpretation of the references to colour in this figure legend, the reader is referred to the web version of this article.)

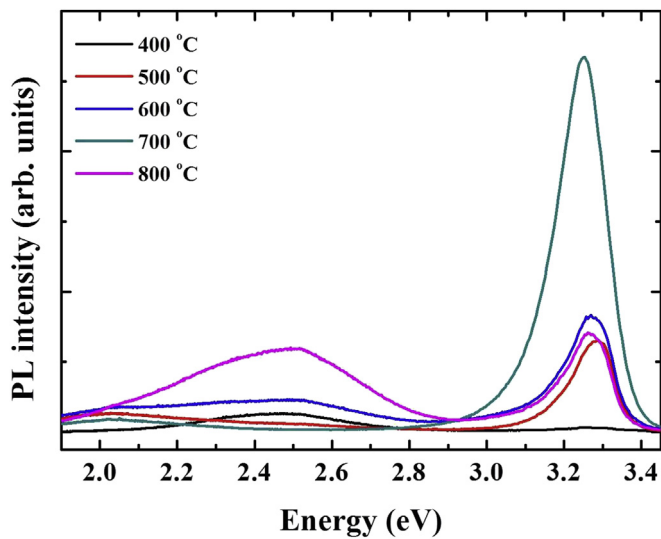


**Fig. 7.** PL spectra of ZnO:In<sup>3+</sup> nanorods prepared using VC-FTFA method at different temperatures.

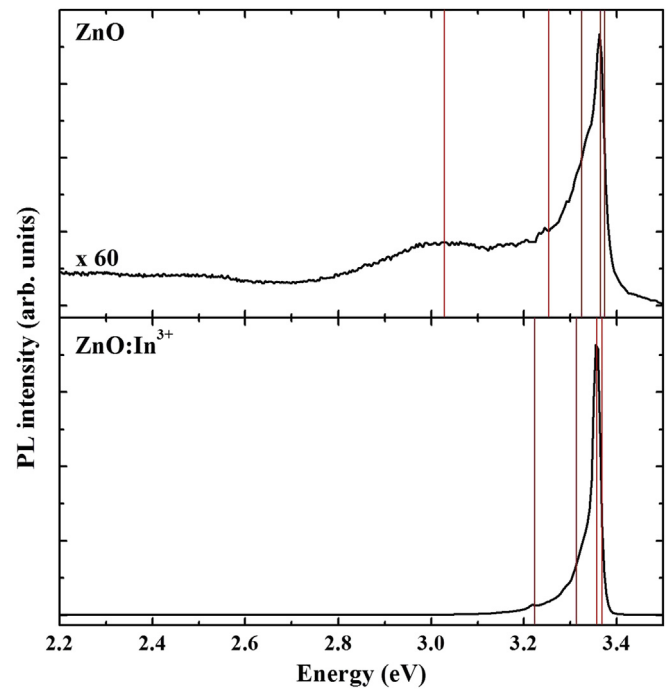


**Fig. 8.** PL spectra obtained at 12 K from undoped ZnO films annealed in open air (upper panel) and from sample 3 (lower panel).

electron-hole pairs as described by Ref. [44].

$$I = I_0 / [1 + C \exp(-\Delta E_A / k_B T)], \quad (9)$$

where  $I$  and  $I_0$  are the integrated intensities of the emission band,  $C$  is a constant,  $k_B$  is Boltzmann's constant, and  $\Delta E_A$  is the activation energy for thermal quenching. Equation (9) highlights the advantage of a large exciton binding energy for certain applications. Indeed, the PL intensity is maximal when the Boltzmann factor in the denominator is zero, i.e. when the activation energy (binding or localization) becomes much greater than the thermal energy. Fig. 9(c) shows the PL intensity of the D<sup>0</sup>X and FX peaks as a function of inverse temperature for sample 3, along with fits of the experimental data to Equation (9) using activation energies of 15

and 62 meV for the D<sup>0</sup>X and FX intensities, respectively. These activation energies are in agreement with the properties derived from the PL spectrum in Fig. 8. Indeed, the D<sup>0</sup>X peaks at  $T < 75$  K originate from the recombination of the donor-bound excitons with a localization energy of 15 meV, a value identical to the localization energy obtained from Fig. 8, while the FX peaks at  $T > 75$  K originate from the recombination of free excitons with a binding energy of 62 meV, a value very close to the exciton binding energy of ZnO (60 meV).

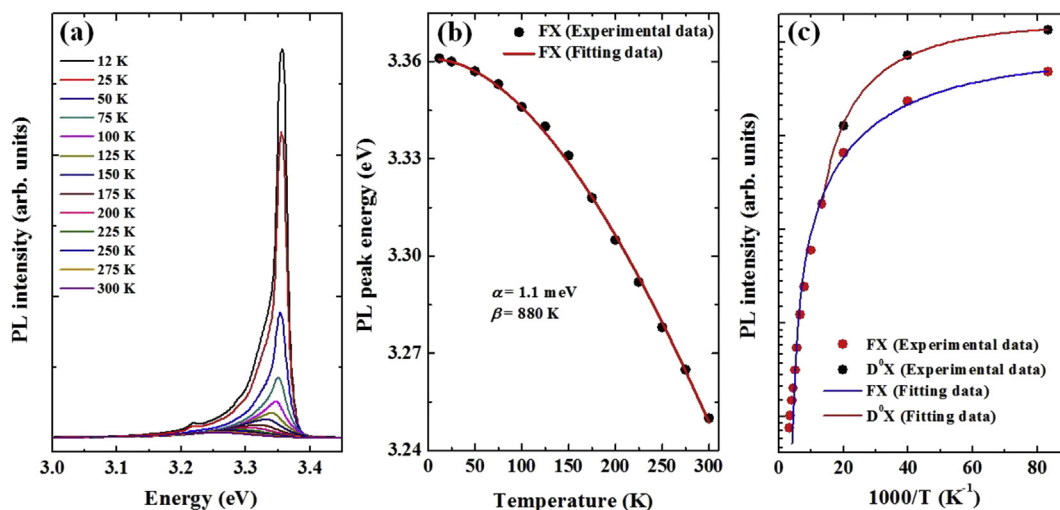


**Fig. 9.** (a) Temperature-dependent PL spectra of NBE emissions of sample 3. (b) The bandgap energies of FX as a function of temperature. The solid line indicates fitting on the basis of Varshni equation. (c) Integrated dependence of PL intensity on temperature. The solid lines are fits to  $I_0/[1 + \text{Cexp}(-\Delta E_A/k_B T)]$  (Equation (9) in the main text).

#### 4. Conclusions

In summary,  $\text{ZnO}:\text{In}^{3+}$  nanorods prepared using VC-FTFA exhibit significantly enhanced PL properties compared with  $\text{ZnO}:\text{In}^{3+}$  and undoped ZnO films annealed in open air. The regrowth of the  $\text{ZnO}:\text{In}^{3+}$  nanorods was due to the chloride-containing metal; here indium chloride, which generated  $\text{ZnCl}_2$  and  $\text{InCl}_3$  vapors. The  $\text{ZnO}:\text{In}^{3+}$  nanorods evolve via a vapor-solid mechanism whereby growth occurs through oxidation of Zn vapor, which then condenses.  $\text{ZnCl}_2$  and  $\text{InCl}_3$  vapors were generated in the temperature region of 390–640 °C, and round-shaped nanoparticles were regrown by the  $\text{ZnCl}_2$  and  $\text{InCl}_3$  vapors. The regrowth afforded by VC-FTFA is effective in increasing both the intensity and the uniformity of the NBE emission. The VC-FTFA method offers a low-coat fabrication route for optoelectronic devices with high external efficiency.

#### Acknowledgments

This research was supported by Global Ph.D Fellowship Program through the National Research Foundation of Korea (NRF) funded by the Ministry of Education (No. 2014H1A2A1018051).

#### References

- [1] H. Jeong, D.J. Park, H.S. Lee, Y.H. Ko, J.S. Yu, S.-B. Choi, D.-S. Lee, E.-K. Suh, M.S. Jeong, *Nanoscale* 6 (2014) 4371–4378.
- [2] T. Singh, T. Lehnen, T. Leuning, D. Sahu, S. Mathur, *Appl. Surf. Sci.* 289 (2014) 27–32.
- [3] D. He, S. Sheng, J. Yang, L. Chen, K. Zhu, X. Feng, *J. Am. Chem. Soc.* 136 (2014) 16772–16775.
- [4] S. Ameen, M.S. Akhtar, H.-K. Seo, M.K. Nazeeruddin, H.-S. Shin, *J. Phys. Chem. C* 119 (2015) 10379–10390.
- [5] Y.-C. Chang, *Catal. Commun.* 56 (2014) 45–49.
- [6] C. Sandoval, O. Marin, S. Real, D. Comedi, M. Tirado, *Mater. Sci. Eng. B-Adv.* 187 (2014) 21–25.
- [7] S. Li, C. Zhang, F. Li, W. Ji, P. Li, M. Ren, P. Wang, M. Yuan, *RSC Adv.* 4 (2014) 24399–24405.
- [8] A. Pescaglini, A. Martin, D. Cammi, G. Juska, C. Ronning, E. Pelucchi, D. Lacopino, *Nano Lett.* 14 (2014) 6202–6209.
- [9] A.M. Lord, M.B. Ward, J.E. Evans, P.R. Davies, N.A. Smith, T.G. Maffei, S.P. Wilks, *J. Phys. Chem. C* 118 (2014) 21177–21184.
- [10] H. Nguyen, C.T. Quy, N.D. Hoa, N.T. Lam, N.V. Duy, V.V. Quang, N.V. Hieu, *Sens. Actuators B Chem.* 193 (2014) 888–894.
- [11] F. Qian, S. Gradecak, Y. Li, C.-Y. Wen, C.M. Lieber, *Nano Lett.* 5 (2005) 2287–2291.
- [12] M.N. Makhonin, A.P. Foster, A.B. Krysa, P.W. Fry, D.G. Davies, T. Grange, T. Walther, M.S. Skolnick, L.R. Wilson, *Nano Lett.* 13 (2013) 861–865.
- [13] M.D. McCluskey, S.J. Jokela, *J. Appl. Phys.* 106 (2009) 071101.
- [14] S.-J. Chang, B.-G. Duan, C.-H. Hsiao, S.-J. Young, B.-C. Wang, T.-H. Kao, K.-S. Tsai, S.-L. Wu, *Phot. Technol. Lett.* 25 (2013) 2043–2046.
- [15] D. Kilian, S. Polster, I. Vogeler, M.P.M. Jank, L. Frey, W. Peukert, *ACS Appl. Mater. Interfaces* 6 (2014) 12245–12251.
- [16] K. Mahmood, H.W. Kang, R. Munir, H.J. Sung, *RSC Adv.* 3 (2013) 25136–25144.
- [17] S. Pati, P. Banerji, S.B. Majumder, *Int. J. Hydrogen Energy* 39 (2014) 15134–15141.
- [18] G.C. Park, S.M. Hwang, J.H. Choi, Y.H. Kwon, H.K. Cho, S.-W. Kim, J.H. Lim, J. Joo, *Phys. Status Solidi A* 210 (2013) 1552–1556.
- [19] M. Benhaliliba, C.E. Benouis, Z. Mouffak, Y.S. Ocaik, A. Tiburcio-Silver, M.S. Aida, A.A. Garcia, A. Távira, A.S. Juárez, *Superlattice Microstruct.* 63 (2013) 228–239.
- [20] S. Kim, S.-h. Lee, J.S. Kim, D.Y. Kim, S.-O. Kim, J.-Y. Leem, *Electron. Mater. Lett.* 9 (2013) 509–512.
- [21] M. Rezapour, N. Talebian, *Ceram. Int.* 40 (2014) 3453–3460.
- [22] Z.-F. Shi, Y.-T. Zhang, X.-P. Cai, H. Wang, B. Wu, J.-X. Zhang, X.-J. Cui, X. Dong, H.-W. Liang, B.-L. Zhang, G.-T. Du, *CrystEngComm* 16 (2014) 455–463.
- [23] R. Zhu, W. Zhang, C. Li, R. Yang, *Nano Lett.* 13 (2013) 5171–5176.
- [24] J.-L. Hou, S.-J. Chang, T.-J. Hsueh, C.-H. Wu, W.-Y. Weng, J.-M. Shieh, *Prog. Photovolt. Res. Appl.* 21 (2013) 1645–1652.
- [25] T. Shinaqawa, M. Izaki, *RSC Adv.* 4 (2014) 30999–31002.
- [26] X. Pu, J. Liu, J. Liang, X. Yusheng, W. Feng, Y. Wang, X. Yu, *RSC Adv.* 4 (2014) 23149–23154.
- [27] H. Kanber, R.J. Cipolli, W.B. Henderson, J.M. Whelan, *J. Appl. Phys.* 57 (1985) 4732–4737.
- [28] G. Nam, B. Kim, Y. Park, S. Park, J. Moon, D.Y. Kim, S.-O. Kim, J.-Y. Leem, *J. Mater. Chem. C* 2 (2014) 9918–9923.
- [29] G. Nam, Y. Park, I. Ji, B. Kim, S.-h. Lee, D.Y. Kim, S. Kim, S.-O. Kim, J.-Y. Leem, *ACS Appl. Mater. Interfaces* 7 (2015) 873–879.
- [30] F. Paraguay, D.W. Estrada, L.D.R. Acosta, N.E. Andrade, M. Miki-Yoshida, *Thin Solid Films* 350 (1999) 192–200.
- [31] C.-C. Lin, Y.-Y. Li, *Mater. Chem. Phys.* 113 (2009) 334–337.
- [32] Y.G. Wang, S.P. Lau, X.H. Zhang, H.H. Hng, H.W. Lee, S.F. Yu, B.K. Tay, *J. Cryst. Growth* 259 (2003) 335–342.
- [33] Ü. Özgür, Ya I. Alivov, C. Liu, A. Teke, M.A. Reshchikov, S. Doğan, V. Avrutin, S.-J. Cho, H. Morkoc, *J. Appl. Phys.* 98 (2005) 041301.
- [34] K. Johnston, M.O. Henry, D. McCabe, E. McGlynn, M. Dietrich, E. Alves, M. Xia, *Phys. Rev. B* 73 (2006) 165212.
- [35] H.-M. Chiu, Y.-T. Chang, W.-W. Wu, J.-M. Wu, *ACS Appl. Mater. Interface* 6 (2014) 5183–5191.
- [36] S. Lin, Z. Ye, H. He, Y. Zeng, H. Tang, B. Zhao, L. Zhu, *J. Cryst. Growth* 306 (2007) 339–343.
- [37] S. Lin, H. He, Z. Ye, B. Zhao, J. Huang, *J. Appl. Phys.* 104 (2008) 114307.
- [38] C. Liu, H. He, L. Sun, Q. Yang, Z. Ye, L. Chen, *Solid State Commun.* 150 (2010) 2303–2305.
- [39] S.P. Watkins, Z.W. Deng, D.C. Li, H. Huang, *J. Appl. Phys.* 110 (2011) 083506.
- [40] H.P. He, H.P. Tang, Z.Z. Ye, L.P. Zhu, B.H. Zhao, L. Wang, X.H. Li, *Appl. Phys. Lett.* 90 (2007) 023104.
- [41] Y.P. Varshni, *Physica* 34 (1967) 149–154.
- [42] N. Kumar, R. Kaur, R.M. Mehra, *J. Lumin.* 126 (2007) 784–788.
- [43] T.-H. Fang, S.-H. Kang, *J. Appl. Phys.* 105 (2009) 113512.
- [44] F. Schuster, B. Laumer, R.R. Zamani, C. Magen, J.R. Morante, J. Arbiol, M. Stutzmann, *ACS Nano* 8 (2014) 4376–4384.